

# The Role of Interfaces on the Deformation Mechanisms in Bimodal Al Laminates Produced by Accumulative Roll Bonding

Heinz-Werner Höppel,<sup>\*</sup> Martin Westermeyer, Frank Kümmel, and Mathias Göken

Laminated metallic materials with an ultrafine-grained (UFG) microstructure can easily be produced by accumulative roll bonding (ARB). Combining two different Al alloys, commercially pure (CP) and high-purity (HP) aluminum, a layerwise bimodal microstructure is formed, where the CP layers consist of ultrafine grains whereas the HP layers show large grains as these layers undergo dynamic recrystallization during rolling. By applying different numbers of ARB passes and in addition by applying a subsequent heat treatment, the microstructure of the laminate can be changed significantly. Thus, different types of interfaces, specifically the grain boundaries of the ultrafine grains and the interfaces between the different layers of CP and HP aluminum are dominating the deformation behavior and the mechanical properties of these laminates. This article addresses how the UFG boundaries and the layer interfaces affect the mechanical properties under monotonic and cyclic loading, and discusses the relevant deformation mechanisms.

bonding (ARB) is one of the most prominent processes used to this end. The ARB process, which was invented by Saito et al. in 1998,<sup>[3,4]</sup> allows to produce UFG sheet materials on standard rolling mills. Furthermore, upscaling of the process seems to be rather straightforward.<sup>[5,6]</sup> The principal of ARB is that two sheets of the same material are rolled together, with the contact surfaces being wire-brushed to remove surface oxidation and contamination. During the thickness reduction in the rolling mill, which is typically 50%, a cold-welding process leads to a binding of the individual sheet layers. Ending up with a sheet thickness identical to the starting conditions, the process can be repeated several times. Through this repeated plastic deformation, a pronounced subgrain structure evolves during the first ARB passes


## 1. Introduction

Since the pioneering work of Gleiter,<sup>[1,2]</sup> the potential of nanocrystalline (NC) or ultrafine-grained (UFG) microstructures to significantly improve the mechanical properties of materials has been widely recognized. In this course, research on UFG/NC materials has been strongly intensified and became rather popular during the last two decades. Besides the bottom-up approach such as inert gas condensation, top-down approaches such as severe plastic deformation processes turned into focus, as these methods allow to produce UFG materials in larger dimensions and quantities. Among others, accumulative roll

within the original grains. With further ARB processing, some of the subgrain boundaries are converted into high-angle grain boundaries (HAGB), leading to a UFG microstructure (for example, see studies<sup>[7,8]</sup>).

UFG/NC microstructures are well known to exhibit extraordinary mechanical properties under monotonic loading. This significant increase in strength sometimes even goes together with enhanced ductility, also known as the “paradox of strength and ductility.” Such an effect has been described so far for equal channel angular pressing (ECAP)-processed Cu, Ti, and Al<sup>[9–11]</sup> as well as for ARB-processed UFG materials.<sup>[12–14]</sup> A possible explanation for the enhanced ductility and the also enhanced strain-rate sensitivity (SRS) in the case of face-centered cubic materials is that thermally activated annihilation of dislocations at the grain boundaries takes place, as reported in the previous studies.<sup>[8,15]</sup> Thus, the grain boundaries seem to play a dominant role in the observed deformation behavior. However, besides the UFG/NC microstructure, also the layer interfaces contribute to the mechanical behavior of the ARB-processed materials. In this context, it has to be pointed out that the ARB process also allows for the combination of different materials, resulting in so-called “heterogeneous laminated materials” or “laminated metallic composites” (LMCs). The properties of LMCs have been already intensively investigated, documented, for example, in a review from Lesuer et al.<sup>[16]</sup> However, these laminates have been produced by processes different than ARB. In contrast to those laminates, ARB-processed LMCs allow for the combination of the beneficial effects of a laminated structure with those from

Dr. H.-W. Höppel, M. Westermeyer, F. Kümmel,<sup>[†]</sup> Prof. M. Göken  
 Department of Materials Science & Engineering  
 Institute I: General Materials Properties  
 Friedrich-Alexander-Universität Erlangen-Nürnberg  
 Martensstr. 5, Erlangen 91058, Germany  
 E-mail: hwe.hoepfel@fau.de

 The ORCID identification number(s) for the author(s) of this article can be found under <https://doi.org/10.1002/adem.202000145>.

<sup>[†]</sup>Present address: Heinz Maier-Leibnitz Zentrum (MLZ), TU München, Lichtenbergstr. 1, Garching 85748, Germany

© 2020 The Authors. Published by WILEY-VCH Verlag GmbH & Co. KGaA, Weinheim. This is an open access article under the terms of the Creative Commons Attribution License, which permits use, distribution and reproduction in any medium, provided the original work is properly cited.

DOI: 10.1002/adem.202000145

a UFG microstructure. Moreover, the process also allows for the design of a sheet architecture by varying stacking order, layer materials, layer thickness, and the number of interfaces.<sup>[17–19]</sup> Consequently, these laminates exhibit an UFG microstructure, combined with a layered structure on the meta-scale. Thus, the question arises, how do the different interfaces, i.e., the grain boundaries and the layer interfaces affect the mechanical properties and the deformation behavior. In this context, materials with bimodal grain structures are highly interesting. As an example, it was found in bimodal copper/bronze LMCs that the material interfaces play a crucial role in mechanical behaviors of the sheets.<sup>[20,21]</sup> In these LMCs, extra geometrically necessary dislocations are present in the vicinity of the material interfaces, which are due to a non-uniform strain gradient resulting from a mechanical incompatibility across the layer interfaces.

In this work, we selected two Al alloys, namely, high-purity (HP) Al 99.999 and commercially pure (CP) Al 99.5 as the two different materials. While very similar materials, they do exhibit significantly different recrystallization behaviors, especially at the processing temperatures. From earlier investigations,<sup>[22]</sup> it is known that during ARB processing of 1 mm thick Al 99.5 and Al 99.999 sheets for up to ten cycles, the Al 99.999 layer recrystallizes (meta-)dynamically, and thus, a layerwise distributed bimodal grain structure within the laminate is received. The layers with commercial purity become UFG with increasing number of ARB cycles. In the HP layers, the grain size does not change during the first cycles. Due to the HP and absence of defects, dislocation and grain boundary movement are not obstructed by atoms, precipitates, or intermetallic phases. For this reason, the grain structure is coarsened by meta-dynamic recrystallization during rolling and cooling of the sheet.<sup>[23]</sup> Only after four cycles, the grain size decreases in the HP layers, as the grain growth is limited in the normal direction by the decreasing layer thickness.<sup>[22]</sup> Ruppert et al.<sup>[24]</sup> used the same material system but produced laminates with five times thicker layers than the material investigated by Chekhonin et al.<sup>[22]</sup> It turned out that for the thicker laminates, the grain size in the HP layers only decreases after six ARB cycles. Using those thicker laminates, Ruppert et al. succeeded in determining the mechanical properties by macroscopic strain-rate compression jump tests and by local strain-rate jump tests using nanoindentation. The macroscopically determined enhanced SRS was found to be a consequence of the deformation behavior of the UFG CP layers, whereas the HP layers do not show a pronounced SRS.

In addition to grain size, the evolution of texture during ARB and subsequent annealing has to be considered. As the HP layer recrystallizes dynamically and the CP layer becomes UFG, different texture components evolve: The UFG layer is preferably S-oriented, whereas the HP layer shows a cube texture component, which is typical for recrystallized aluminum.<sup>[22]</sup> Lienshöft et al.<sup>[25]</sup> also showed that the grain size and the texture can be significantly changed by a post-ARB heat treatment at 300 °C or, respectively, at 400 °C for 1 h.

Under cyclic loading, it is well known that UFG structures exhibit enhanced fatigue life in a Wöhler-(SN)-diagram when compared with their conventionally grain-sized (CG) counterparts.<sup>[26,27]</sup> However, a deterioration of the low cycle fatigue (LCF) life is observed when the total strain or Coffin–Manson fatigue life diagrams are regarded.<sup>[28–32]</sup> It is also well known that

introducing a bimodal grain structure by subsequent heat treatment can significantly improve the LCF life, however, on the expense of a deteriorated fatigue life in the SN plot.<sup>[33,34]</sup> There is no investigation available so far, how a layerwise bimodal microstructure affects the fatigue lives.

Thus, the selection of materials in combination with subsequent heat treatments offers an ample opportunity to change the grain structure and investigate the contributions of the different interfaces to the mechanical deformation behavior under monotonic and cyclic loads. A detailed understanding of the impact of different structural features on the mechanical properties and the deformation mechanisms is not yet developed. Thus, this article addresses how the UFG boundaries and the layer interfaces affect the mechanical properties under monotonic and cyclic loading, and discusses the relevant deformation mechanisms.

## 2. Results and Discussion

**Figure 1** shows the alternating structures of the different laminates in a cross-sectional view. It can be clearly seen that with an increasing number of ARB cycles, the HP layers are stacked more tightly. It is also apparent that, for the condition with the most rolling passes (N9), the grain size in the HP layers along the normal direction is limited by the layer thickness.

To reveal the different textures that evolve during ARB processing or during subsequent annealing, electron backscatter diffraction (EBSD) measurements have been performed. To analyze the CP and HP layers in an efficient manner, the layers were analyzed separately due to their large difference in grain size; see **Figure 2** and **3**.

In **Figure 2**, a significant reduction in grain size from four to nine ARB cycles is evident. Furthermore, shear bands are visible in the N7 and N9 conditions, and the  $\langle 101 \rangle$  texture becomes more pronounced; see also the displayed pole figures in **Figure 3**. In addition, the annealing treatment at 250 °C for 1 h leads to a significantly coarser grain structure and a stronger pronounced  $\langle 101 \rangle$  texture when compared with the as-rolled (AR) condition. It is also found that the grain structure of the HP layers grows about 1 μm into the CP domains. During annealing at 300 °C for 1 h, most of the UFG grains recrystallize, and thus, the grain size increases. For the N4 condition, some smaller ultrafine grains still remain. However, the amount of remaining ultrafine grains in the CP layers diminishes strongly for the N7 and N9 conditions, as can be seen in **Figure 4**. Here, it also becomes obvious that due to recrystallization, the pronounced  $\langle 101 \rangle$  texture disappears and the  $\langle 100 \rangle$  cube texture components become dominant, as observed in the corresponding pole figures of the CP layers in **Figure 3a–c** for the different conditions.

**Figure 4** shows the evolution of the grain structure and orientation for the HP layers. Already in the AR condition, a pronounced  $\langle 100 \rangle$  cube texture is dominant. This not only holds true for the N7 and N9 conditions but also for the N4 condition. The grain size along the rolling direction stabilizes at N7. However, whereas for the N7 condition, each HP layer consists of about two to three grains along the normal direction for the N9 condition, and one single grain spans over the complete layer thickness. This is sometimes also denoted as a columnar grain structure. Annealing at 250 °C again leads to a moderate increase

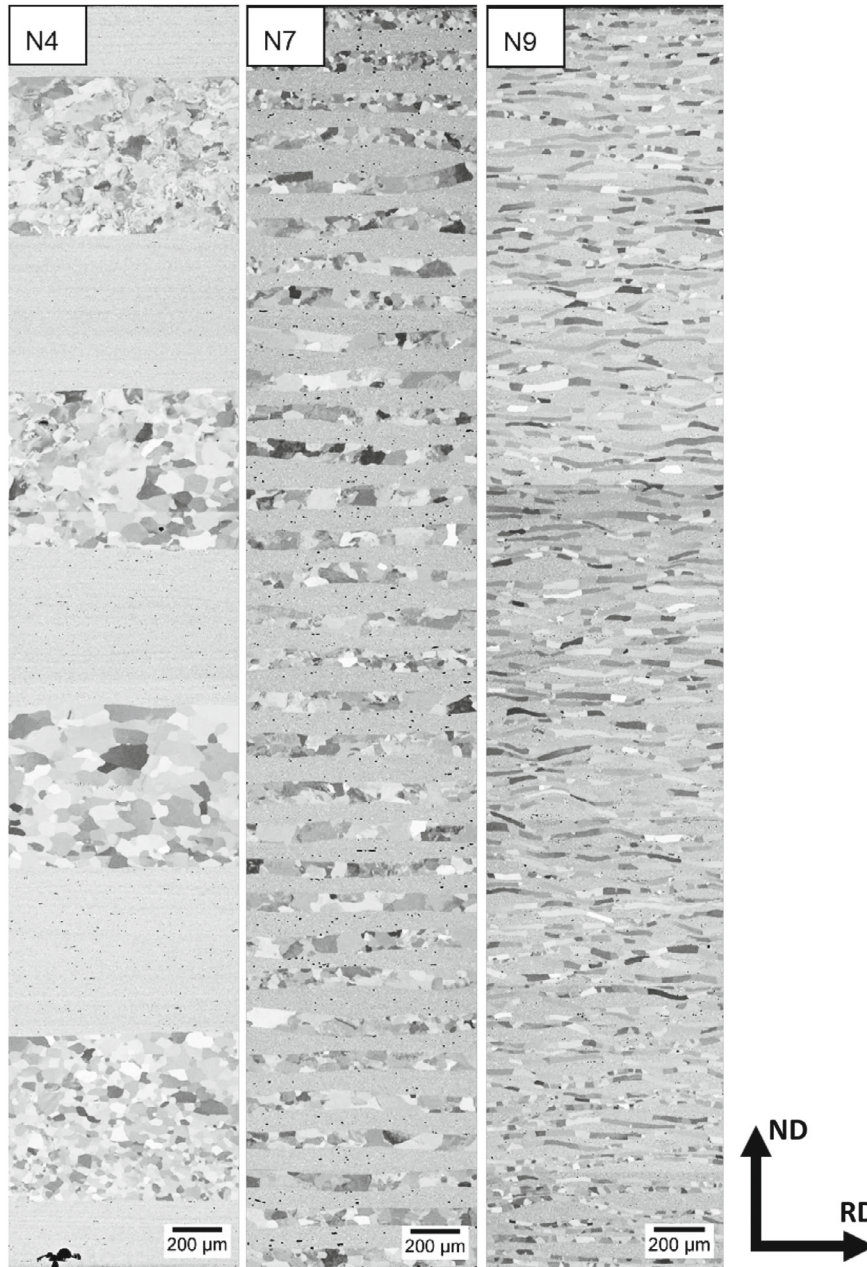


**Figure 1.** Cross-sectional view of the laminate structures after four, seven, eight, and nine ARB cycles in the AR conditions (ND: Normal direction, RD: Rolling direction).

in grain size for the N4 and N7 conditions. However, it appears that for the N9 condition, no significant change in grain size is visible. Annealing at 300 °C results in pronounced grain growth, and the thickness of the UFG CP layers decreases significantly for the N7 condition. For the N9 condition, the UFG CP layers almost completely disappear.

The above-mentioned behavior observed for the CP and HP layers fits well to the observations of Lienshöft et al.<sup>[25]</sup> A calculation of the diffusion profiles of Si and Cu in aluminum at 300 °C and 1 h annealing time using ThermoCalc software reveals that the maximum diffusion length of Si amounts to 3.5 μm and that of Cu to 1.3 μm. In this context, it has to be noted

that the layer thickness of the N9 condition is of a rather similar size. Thus, the growth behavior of the grains from the HP layer into the CP layer appears to be a consequence of the diffusion of solute atoms to the HP layers.

The different structures have also strong impact on the mechanical properties; see **Figure 5** and **6**. When comparing the mechanical behavior of the Al 99.5/Al 99.999 LMCs with the data of CP Al (Al 99.5) in the CG condition and in the UFG condition after four ARB passes, **Figure 5**, two main issues become obvious: 1) The introduction of the UFG microstructure in Al 99.5 leads to a significant increase in the yield strength of the material by more than 400% and of the ultimate tensile

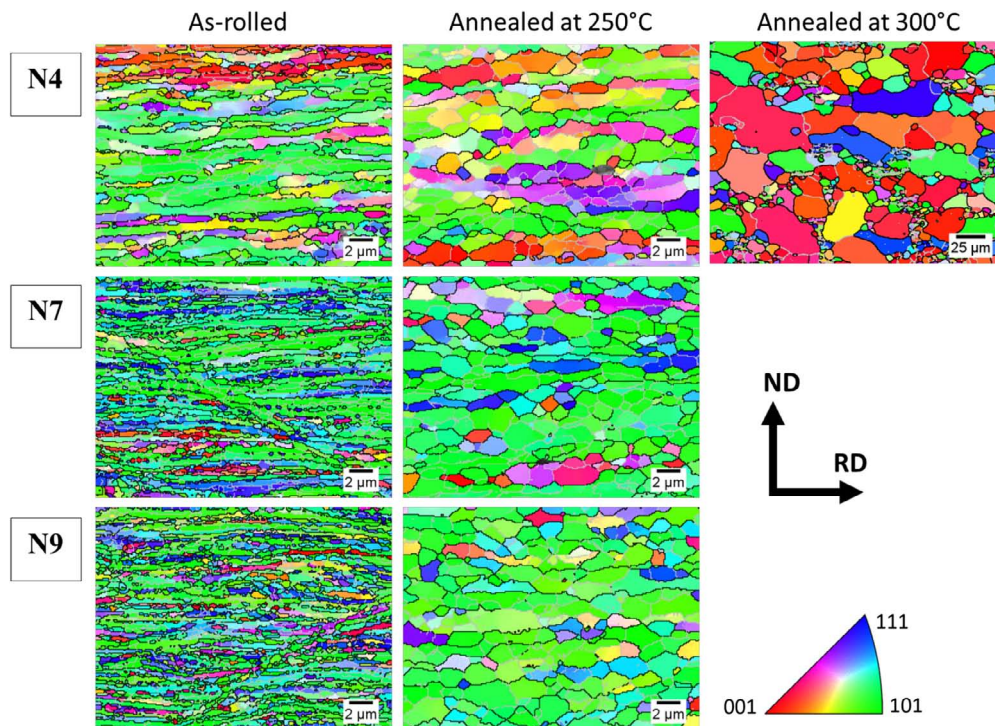


**Figure 2.** EBSD mappings of the CP layers (Al 99.5) in the middle of the sheets for N4, N7, and N9 and for the AR and the conditions annealed at 250 °C or, respectively, 300 °C for 1 h. Inverse pole figure (IPF) in transverse direction (TD).

strength (UTS) by about 250% when compared with the CG counterpart (Al 99.5 N0). However, this increase in strength is at the expense of ductility, as the uniform elongation and the fracture strain are significantly reduced for the UFG material. As noted earlier, it has to be also kept in mind that the deformation behavior of the UFG condition is highly strain rate-dependent. Thus, it is important to compare the mechanical data at the same strain rate, which is done here. The LMCs with their bimodal grain structures exhibit a good compromise between increasing strength and retained ductility. The increase in yield strength amounts to about 300%, whereas the uniform elongation and the fracture strain are only slightly reduced when compared with the CG Al 99.5 behavior. Similar behavior has been reported just recently by Jianga et al.<sup>[35]</sup>

If we take a closer look at the behavior of the LMCs in the AR conditions, Figure 5 and 6a, a pronounced difference in the mechanical properties among N4, N7, and N9 is visible. As already described earlier, the grain size in the N4 condition is significantly coarser than for N7 and N9. Thus, the yield strength and UTS are significantly smaller in the N4 condition. It also becomes apparent that, although the grain size determined from the EBSD-measurements for the N7 and N9 conditions is similar, the N7 condition shows a higher yield strength but due to a lower work hardening a smaller UTS compared with the N9 condition.

Results from nanoindentation tests reveal that the hardness of the HP layer of 0.4 GPa in the AR condition is roughly three times smaller than that of the CP layer with a hardness of 1.15 GPa. Thus, yielding will start in the weaker HP layers, and the small differences in the texture of the CP layers with increasing number of ARB passes cannot account for that. However, for the N9

condition with a columnar grain structure in the HP layers, the number of interfaces between the HP and CP layers is by a factor of 4 higher compared with the N7 condition. Obviously, the character of the interface seems to have a significant influence on the yielding and work hardening behavior: In the N7 condition, the HP layer exhibits two to three grain boundaries (grain boundary interfaces) across the thickness of the layer and 127 HP-/CP-layer interfaces. In contrast, in the N9 condition, the grain boundary interfaces (across the layer) are absent in the HP layers, but the number of layer interfaces increases to 511. It has also to be mentioned that the fraction of HAGB is increasing from 62% for N4 to 67% for N7 and 72% for N9, which might also slightly influence the mechanical behavior.

After an annealing treatment at 300 °C for 1 h, the differences among the N4, N7, and N9 conditions completely disappear. The material becomes rather soft, and work hardening is identical for all conditions. This is in agreement with the microstructural observations described earlier. This particular annealing treatment ends up in rather similar microstructures, resetting all the differences introduced by the different ARB cycles.

In contrast, the annealing treatment at 250 °C leads to a more complex situation. Due to the larger grains compared with the AR conditions, the yield strength is significantly smaller. However, work hardening is almost identical for N4 and N7, but higher for N9. Through a closer look to the yielding regime, Figure 6b, pronounced differences in the yielding behavior can be seen. The N4 and N7 conditions show the typical behavior of a material with a yield point. This behavior completely disappears for the N9 condition. A yield point is also reported for the aluminum alloy AA1100 after annealing by Kwan et al.<sup>[36]</sup>

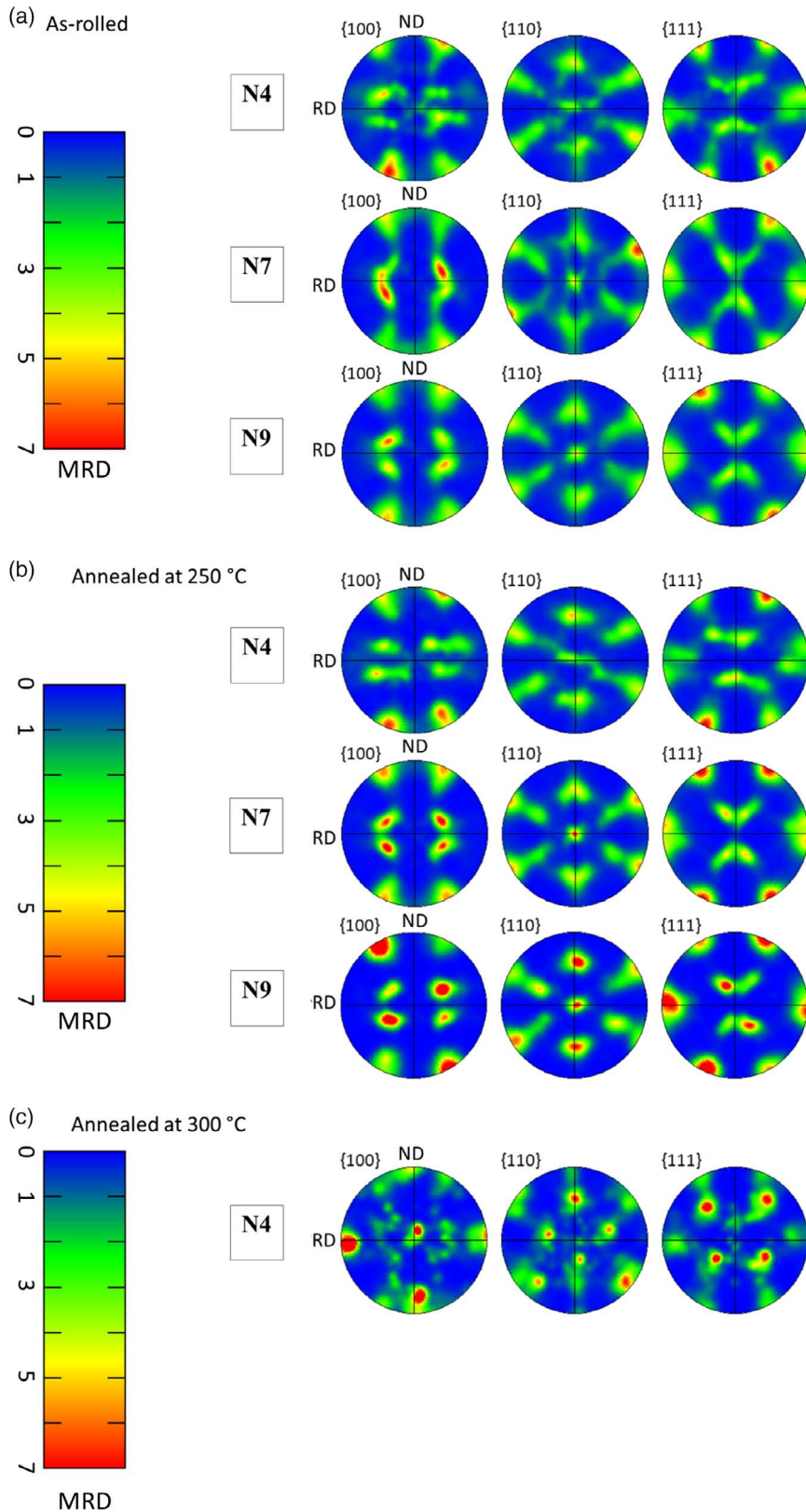


**Figure 3.** Pole figures of the CP layers (Al 99.5) in the middle of the sheets for N4, N7, and N9 and for a) the AR and the conditions annealed at b) 250 °C or, respectively, c) 300 °C for 1 h.

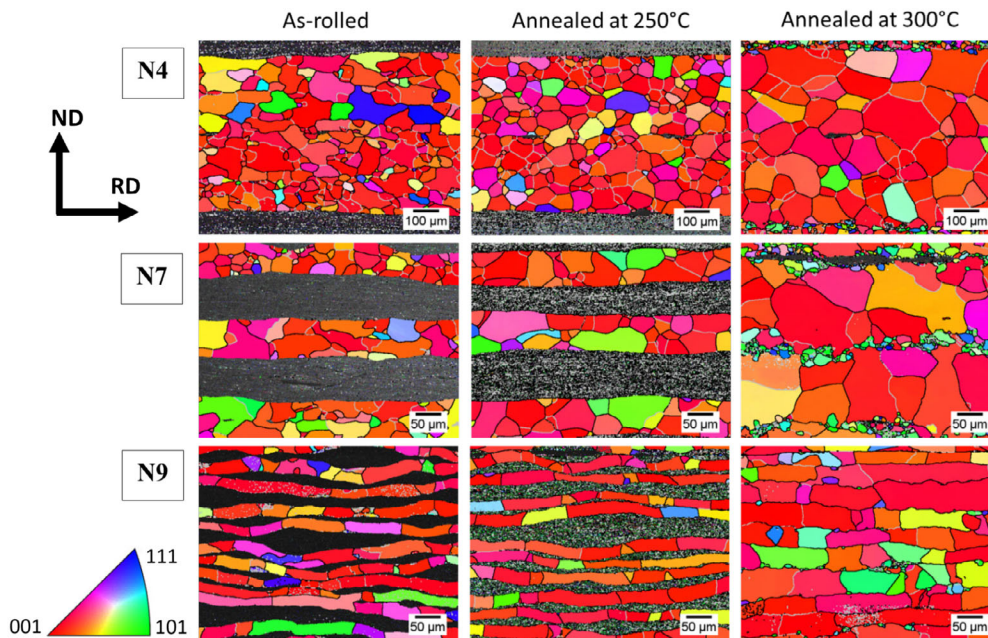


**Figure 4.** EBSD mappings of the HP layers (Al 99.99) in the middle of the sheets for N4, N7, and N9 and for the AR and the conditions annealed at 250 °C or, respectively, 300 °C for 1 h. IPF in TD.

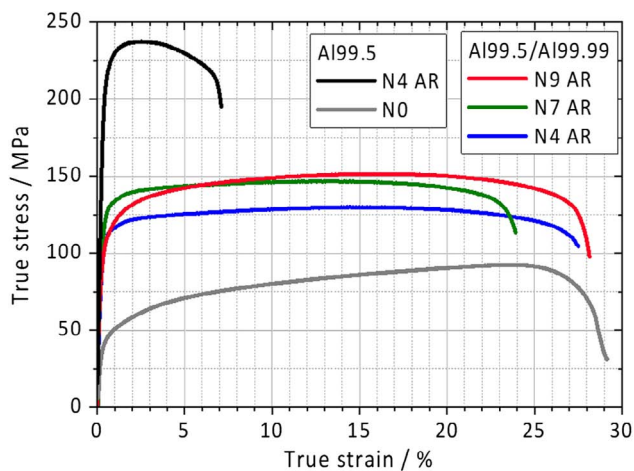


**Figure 5.** True stress–true strain diagram for N4, N7, and N9 in the AR conditions at a strain rate of  $10^{-3} \text{ s}^{-1}$ . For comparison stress–strain data for CP Al 99.5 in the conventionally grained (N0) and UFG (N4) conditions are also plotted.

As yielding is at the beginning of the tensile test still localized to the softer HP layers, the interface character plays a significant role in the yielding behavior. It is also most interesting that the N4 condition shows a higher yield strength than the N9 condition.

A pronounced yield strength is obtained when initial dislocation motion is hindered by the interaction of solute atoms with the distortion field of dislocations. This so-called Cottrell clouds<sup>[37]</sup> are typical for annealed materials, where interstitials diffuse to energetically favorable positions where the lattice is dilated by dislocations. As this effect is well pronounced, equally for the N4 and the N7 conditions after annealing at 250 °C

for 1 h, it can be concluded that neither the grain size nor the number of ARB cycles and, consequently, the different number of interfaces influence this effect. On the other hand, in the N9 condition, pronounced yielding is completely absent.

To understand the observed phenomena in more detail, tensile tests at different strain rates have been performed, **Figure 7a–c**. In the AR states, the N4, N7, and N9 conditions show a pronounced influence of the strain rate, which strongly depends on the number of ARB cycles. The SRS analysis has been performed at 2% strain, where the N7 condition exhibits an SRS  $m$  of 0.035, whereas it equals to 0.022 for N4 and to 0.014 for N9, **Figure 8**. After annealing at 250 °C for 1 h, a strain rate sensitive behavior is still visible; however, the influence of the strain rate becomes less pronounced. The SRS  $m$  for the N4 and N7 conditions declines to 0.013, and for the N9 condition,  $m$  equals 0.006. The strain rate sensitive behavior was also investigated for the N9 condition after annealing at 300 °C for 1 h. As the UFG structure is almost completely lost, the SRS becomes negligible and turns slightly to the negative regime. Mutually, this is a consequence of the diffusion of Si to the HP layers at the high annealing temperature of 300 °C. In **Figure 7d**, a detailed view of the yielding regime is plotted. It turns out that the pronounced yield strength observed for N4 and N7 conditions annealed at 250 °C for 1 h also depends on the strain rate. As expected, with smaller strain rates, pronounced yielding becomes less distinct. On the other hand, for the N9 condition, pronounced yielding is absent for all strain rates.

Bringing all the obtained results together, it becomes obvious that with a higher number of ARB cycles and thus a higher fraction of HAGBs (higher grain boundary volume), the SRS increases, which is most evident in a comparison between the behavior of N4 versus N7. This is well known; see, for example,

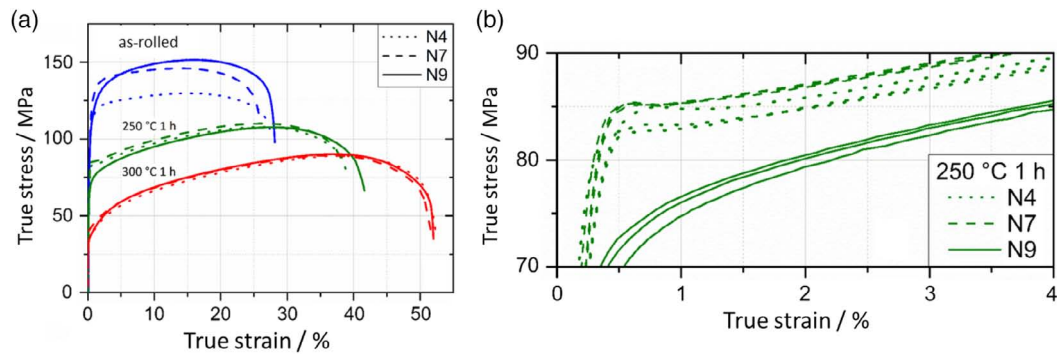


**Figure 6.** a) True stress–true strain diagram for N4, N7, and N9 in the AR (blue) and at 250 °C for 1 h (green) or, respectively, 300 °C for 1 h (red) annealed conditions at a strain rate of  $10^{-3} \text{ s}^{-1}$ . b) Detail at the yielding regime from (a) for the conditions annealed at 250 °C for 1 h. The results of repeated tests are displayed to clearly show that the pronounced yield strength visible for the N4 and N7 conditions is absent for the N9 counterpart.

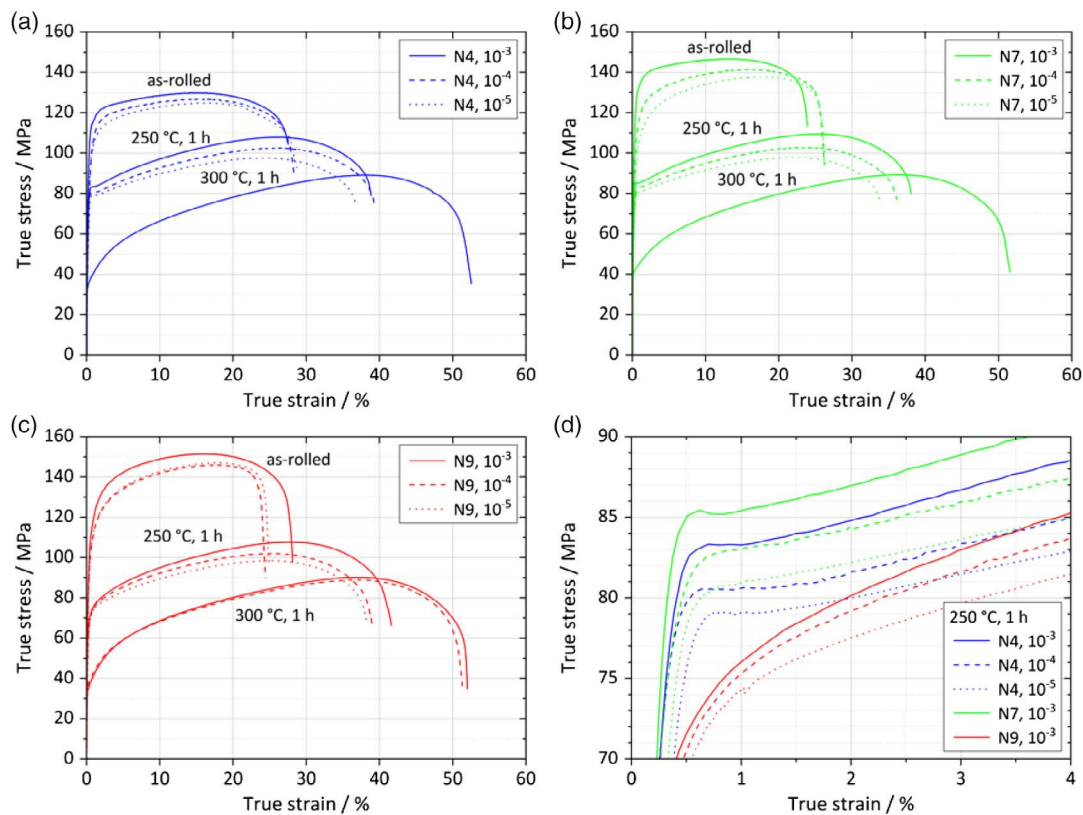


**Figure 7.** True stress–true strain diagrams determined at the different strain rates of  $10^{-3} \text{ s}^{-1}$ ,  $10^{-4} \text{ s}^{-1}$  or, respectively,  $10^{-5} \text{ s}^{-1}$  for a) N4, b) N7, and c) N9 AR and annealed conditions. d) Detailed view on the yielding regime conditions in the AR (blue) and at 250 °C for 1 h (green) or, respectively, 300 °C for 1 h (red) annealed conditions. b) Detail at the yielding regime from (a) for the conditions annealed at 250 °C for 1 h.

the previous study.<sup>[12]</sup> At a first glance, it appears that a high number of layer interfaces, or, respectively, a higher interface density, are counteracting this trend, as the AR N9 condition exhibits almost the same grain size as the N7 condition but the smallest SRS. Annealing at 250 °C leads to pronounced grain growth in the CP layers of all conditions, and thus, the grain size and the grain boundary volume becomes rather comparable (see Figure 2). Consequently, a very similar SRS for the N4 and N7 conditions is obtained. Although the grain size in the CP

layers of the N9 condition is almost identical to the N4 and N7 conditions, Figure 2 and 4, the SRS is smaller. Again, this can be related to the different interface densities, which scales directly with the number of layer interfaces as the total sheet thickness stays almost constant. The number of layer interfaces increases from 15 for the N4, to 127 for the N7 and to 511 for the N9 condition. It has also to be considered that the HP layers in the AR and at 250 °C for 1 h annealed N9 condition exhibit a columnar grain structure; see Figure 4. As the density of the layer

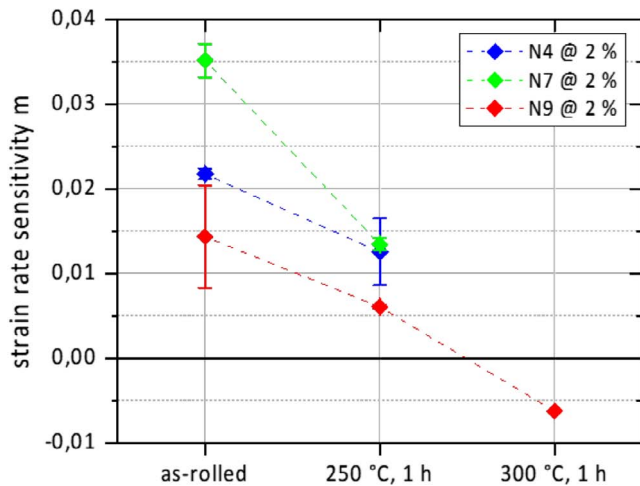


**Figure 8.** SRS for the conditions N4, N7, and N9 in the AR state and after annealing at 250 and 300 °C for 1 h. The analysis was performed at 2% total strain.

interfaces increases by a factor of  $\approx 8$  when the N4 and N7 conditions are regarded, a significant change in the SRS behavior of the conditions annealed at 250 °C should be found. This is not the case. However, the N9 conditions shows a significantly smaller SRS. All N9 conditions on one hand exhibit a significantly higher layer interface density and, on the other hand, a columnar grain structure. It also has to be pointed out that, in this study, the layer thickness directly scales with the number of layer interfaces. Thus, it becomes obvious that if the layer thickness is in the range of the grain size, the deformation behavior is seriously changing. Not only the SRS is reduced but also the yielding behavior and work hardening are affected. As we see in Figure 6b and 7d, the annealed N7 and N4 conditions show a pronounced yield strength and a work hardening behavior that is comparable. The N4 condition is weaker than the N7 condition due to the differences in grain size and HAGB fraction. However, the deformation behavior of the N9 condition is different. In the AR conditions, the yield strength is smaller than for the N7 condition, and the work hardening is stronger; see Figure 6a. The differences between N7 and N9 become even more evident, when the conditions annealed at 250 °C are

regarded. Pronounced yielding is completely absent for the N9 condition, and work hardening is much stronger than for the N7 and N4 counterparts. Again, it has to be emphasized that the main difference in the microstructure of the annealed conditions is the higher density of layer interfaces combined with the columnar grain structure. The number and thus the density of layer interfaces remain unchanged during annealing. However, diffusion of impurity elements such as Si and Cu from the CP to the HP layer takes place. It is well known that at moderate temperatures, pipe diffusion along grain boundaries and other lattice defects such as dislocations is more effective than volume diffusion. Thus, in the N4 and N7 condition, mutual diffusion of Si and, to some extent, Cu from the CP to the HP layer via pipe diffusion along grain boundaries and dislocation cores leads to an interplay between first dislocation motion and impurities, explaining the existence of the pronounced yield points.

However, in the N9 condition, where a columnar grain structure exists, a pronounced yielding behavior is absent, yielding takes place at lower stresses, and work hardening is more strongly pronounced. This observed behavior can be explained as follows: The columnar grain structure leads to a significantly smaller grain boundary density in the interior of the HP layers. Moreover, it also allows dislocation loops to expand more easily from the grain interior, which are subsequently stored at the layer interfaces. Thus, pipe diffusion of impurity elements along grain boundaries and dislocation cores in the HP layers is retarded. Consequently, the interplay between initial dislocation motion and impurity atoms is absent. The observation that for the AR N9 condition, where the number of layer interfaces is four times higher than for the N7 condition, the yield strength is smaller and the work hardening is higher than for the N7 counterpart, support this explanation. Also, the lower SRS of the AR N9 condition indicates a different arrangement of dislocations at the layer interfaces when compared with the N7 counterpart. The scheme in **Figure 9** displays the main differences.

Internal stresses might also contribute to the overall behavior. Due to the different strengths of the HP and CP layers, strain gradients at the layer interfaces and resulting from that internal stresses will evolve during ARB processing. Depending on the microstructure of the HP layer internal stresses will develop differently. With smaller layer thickness and also, to some extent, due to the columnar grain structure that forms (especially, N9

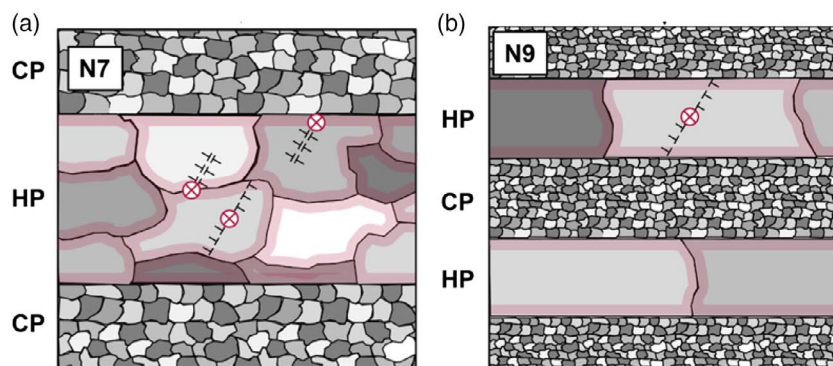


**Figure 9.** Scheme of the different meta-microstructures: a) N7 condition and b) N9 condition. The magenta-colored boundaries reflect for the diffusion zones after annealing at 250 °C. Please mind that the layer thickness in (a) is four times thicker than the layer thickness in (b).



condition), the volume fraction of a grain that is affected by internal stress gradients increases. Consequently, initial dislocation motion can be shifted from the regions close to the layer interfaces more toward to the grain interior where impurities are still absent. Similar findings have been reported for Cu/brass LMCs by the previous studies.<sup>[20,21]</sup>

However, further in-depth investigations are necessary to give proof for the above-mentioned considerations.

When cyclic loading is regarded, the AR N9 and N7 conditions show significantly higher fatigue lives than the Al 99.5 mono-materials in the CG (N0) and the UFG (N4) condition, **Figure 10a**. It also turns out that the UFG grain structure alone has a beneficial effect on the fatigue life, as it is already well reported in the literature; see the previous studies.<sup>[26,27]</sup> The improved fatigue lives of the LMCs in the LCF regime are a consequence of the higher ductility, as already discussed for the monotonic tensile tests. Data for the HCF regime are currently missing. However, a crossover of the fatigue life curves of the Al 99.5 N4 condition with the LMCs will occur as the strength of the LMCs is smaller than for the Al 99.5 N4 material. This explanation fits very well with the principal considerations made by Mughrabi and Höppel,<sup>[28]</sup> where a crossover of the total strain fatigue life curves is motivated by the changes of the fatigue ductility and fatigue strength coefficients of the Coffin–Manson and Basquin laws when comparing CG and UFG microstructures.

When we take a closer look to the different behaviors of the LMCs alone, **Figure 10b**, the N7 AR condition shows the highest fatigue life in a Wöhler–SN-curve followed by the N9 counterpart. Annealing at 250 °C or, respectively, 300 °C leads to a significant drop in the fatigue lives compared with the AR conditions. The higher fatigue lives of the N7 conditions compared with the N9 counterparts are somehow surprising, as the determined mechanical properties under monotonic loads are not that systematically different; compare **Figure 6**.

As fatigue lives are the result of a multistage process,<sup>[39]</sup> an analysis of the crack paths in the scanning electron microscope (SEM) helps shed some light on this point, **Figure 11**. In the AR condition, only few cracks form, but the cracks are always strongly deflected at the HP/CP interfaces, **Figure 11a**. Instead, in the annealed conditions, many cracks formed along 45° to the loading axis, and they are surpassing the HP/CP interfaces without any deflection, **Figure 11b,c**. The increased fatigue lives of the N7 condition compared with the N9 counterpart are a result of the higher layer thickness and also of the higher yield strength: According to Kümmel et al.,<sup>[40,41]</sup> the difference in local yield strength across the layer interface will lead to a deflection of the process zone at the crack tip along the interface, and consequently, the crack is deflected at the interfaces. However, this effect also depends on the layer thickness.<sup>[42]</sup> If the layer thickness is too small, crack bridging will occur.

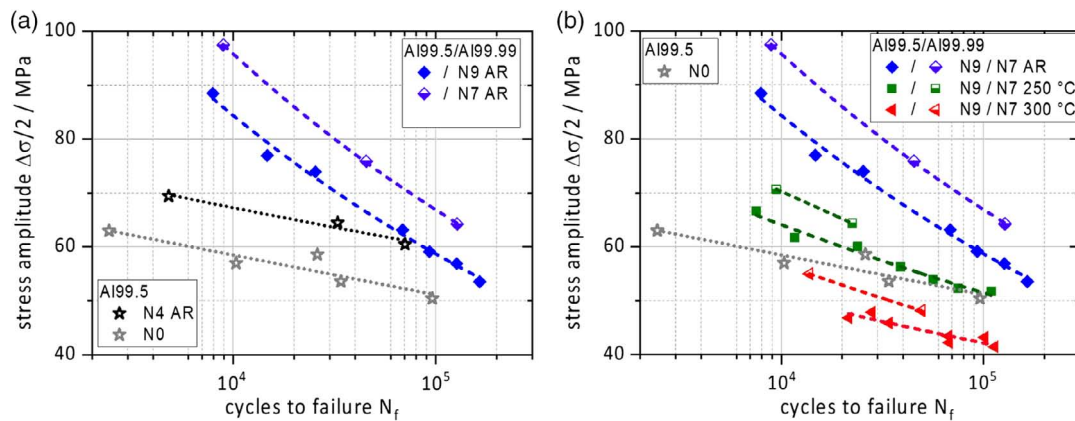
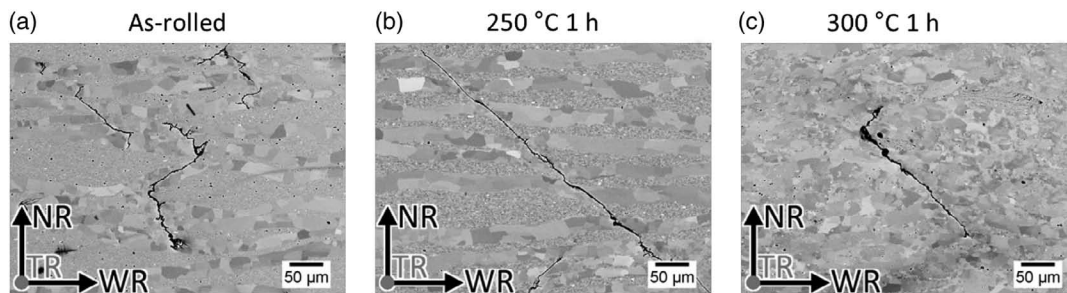


**Figure 10.** a) Wöhler–SN-fatigue life diagram for the AR state of the N9 (full symbols) and N7 (semi-full symbols) condition. Also, data for CP Al 99.5 (N0 and N4 conditions) from the previous study<sup>[38]</sup> are plotted for comparison. b) Overview of the fatigue lives for the AR, and heat-treated conditions of the N9 (full symbols) and N7 (semi-full symbols) states. Data for CP Al 99.5 in the CG (N0) condition are displayed for comparison.



is too small, crack bridging will occur.

**Figure 11.** Different typical crack paths for N9 in the a) AR, b) annealed at 250 °C for 1 h, and c) annealed at 300 °C for 1 h conditions. All specimens were fatigued at a total strain amplitude of  $\Delta\epsilon_{tot}/2 = 1.75 \times 10^{-3}$ .

### 3. Conclusions

Bimodal laminates consisting of HP (Al 99.999) and commercial purity (Al 99.5) aluminum have been produced by the ARB process. During ARB processing, different textures evolve: The UFG CP layers become  $\langle 101 \rangle$  dominated (S-type), whereas the HP layers show a  $\langle 100 \rangle$  cube orientation, which is typical for recrystallized aluminum. A subsequent heat treatment at 250 °C or, respectively, 300 °C for 1 h changes the textures toward a  $\langle 100 \rangle$  cube orientation, and the grain size increases. After the heat treatment at 300 °C, it can be seen that the large grains of the HP layers grow into the fine-grained structure of the technically pure layers. Due to the reduced layer thickness of the N7 and N9 conditions, the grains from the HP layers grow so deeply into the neighboring Al 99.5 layers that they meet at many points in the middle of the layer. Thus, the cube orientation of the Al 99.999 layers spreads. Tensile tests revealed that the yielding and the work hardening behavior are different for the N7 and N9 conditions in the AR state. In the N9 condition, only one grain spans over the complete layer thickness of the HP layer, and this is likely to be responsible for the observed mechanical behavior. For the 250 °C annealed conditions with four or, respectively, seven ARB cycles, it turned out that a pronounced yielding is obtained. Instead, in the N9 condition, this behavior is absent, which is again related to the particular microstructural arrangements of the N9 HP layers. Also, the strain rate sensitive behavior of the N9 conditions differs strongly from the N4 and N7 counterparts. It is concluded that the particular microstructural arrangement of the high number of layer interfaces paired with a columnar grain structure explains the different behavior deformation behaviors of the N9 condition. Fatigue tests revealed that the layer thickness and the annealing treatments significantly affect the fatigue lives.

### 4. Experimental Section

**Materials:** In this investigation, Al sheets of commercial purity (CP: 99.5%) with an original thickness of 5 mm and sheets of Al 99.999% (high purity: HP) were used. The chemical composition of the Al 99.5 was determined by spark optical emission spectroscopy, **Table 1**.

**ARB Processing and Heat Treatments:** The ARB process was applied using a BW 300/350 quarto mill from Carl Wezel company. For details on the ARB process, the reader is referred to Saito et al.<sup>[3]</sup> The working rolls used have a diameter of 90 mm. The tests were carried out at a rolling speed of 8 m min<sup>-1</sup>. The pass reduction was 50% nominally. Before the individual rolling steps, the plates were degreased with acetone and roughened with a rotating steel-wire brush. To prevent the sheets from shifting against each other during rolling, they were joined at the rear end with aluminum rivets. All rolling steps were carried out at room temperature. Due to the large plastic deformation during rolling, the sheet temperature rose to about 70 °C. Between each cycle, the sheets were cooled in air. To achieve the desired layer architectures, we proceeded as follows: In the first cycle, an Al 99.5 was rolled with an Al 99.999 sheet. In the second step, two such sheets were joined together with the Al 99.999 sides without first cutting them into pieces. By omitting the cutting step, the sheet length

**Table 1.** Chemical composition of CP Al (Al 99.5).

Element	Al	Fe	Si	Mg	Mn	Ti	Zn	Cu	Cr
wt%	99.43	0.34	0.11	0.043	0.03	0.024	0.013	0.008	0.002

was doubled, and the portion that had to be cut off at the beginning and end of the sheet during the following rolling cycles was halved. In the subsequent rolling cycles, the sheets were cut before rolling. Due to the symmetrical layer architecture, the stacking sequence is no longer important here. Up to nine ARB cycles have been performed.

To create different states of microstructural recovery starting from the rolling condition, the samples for the microstructure and nanoindentation measurements were heat treated in a circulating air furnace at 250 and 300 °C for 60 min.

**Microstructural Characterization:** The samples for the investigations in the SEM were ground with water cooling up to 4000 grit and, subsequently, mechanically polished with 3 and 1 μm diamond suspension before final mechanical polishing with 0.04 μm silicon oxide suspension (Struers OP-U Nondry). To ensure a deformation-free surface preparation, the final step was electrolytical polishing with Struers A3 electrolyte at -40 °C temperature. To map the microstructure and the fracture surfaces, a Crossbeam 1540 EsB SEM from Zeiss was used. Backscattered electron (BSE) was mainly used for the microstructural imaging. The surfaces of the fatigue samples were imaged with the secondary electron (SE) detector. EBSD measurements were made near the middle of the four, seven, and nine cycles of sheets in the rolled condition and after 1 h heat treatments at 250 and 300 °C. Due to the bimodal grain size distribution in the rolled condition and after the 250 °C heat treatment, it was necessary to measure the different layers individually with optimized parameters. The SEM was equipped with a Nordlys EBSD detector from Oxford Instruments. The working distance was 16 mm, and the acceleration voltage was 20 kV. For the N7 and N9 samples, mappings with a size of 500 × 375 μm<sup>2</sup> were recorded at a measuring point distance of 0.75 μm. To be able to record an entire layer for the N4 samples, the measuring point distance was doubled for the same number of pixels. Because the grains in the Al 99.5 layers are very small in the rolled state and after heat treatment at 250 °C, successful EBSD measurement was not possible even with changed parameters. As a consequence, the measurements of these microstructures were carried out using a Zeiss 540 electron microscope equipped with a NordlysNano EBSD detector (Oxford Instruments). To reduce the size of the scattering volume, the acceleration voltage was reduced to 12.5 kV, and the sample current was limited to 1 nA. The working distance was 6 mm. Mappings with at least 25 × 18 μm<sup>2</sup> were recorded at a step size of 0.1 μm. The indexing rate was about 70%. To have a higher statistical significance for the texture evaluation, either larger mappings were made or several mappings were recorded at the individual samples. After the measurement, the recorded mappings were processed using the EBSD evaluation software from Oxford Instruments. First, in the Tango module, non-indexed points were filled, and small- (2°–15°, gray lines) and large-angle grain boundaries (>15°, black lines) were traced. Then, the grain sizes and the disorientations between the grains were determined. Pole figures as well as inverse pole figures were generated with the software module Mambo.

**Nanoindentation:** To determine the hardness in the individual layers of the laminate, nanoindentation measurements were carried out on the sheets in the rolled state and after heat treatment using a Nanoindenter XP from Nano Instruments Inc. This was equipped with a Berkovich tip and operated in Continuous Stiffness Measurement (CSM) mode.

**Tensile Testing:** The geometry of the tensile test specimens is shown in **Figure 12**. The nominal cross section is 5 × 4.5 mm<sup>2</sup>, and the gauge length is 10 mm.

The specimens were tested at the strain rates of 1 × 10<sup>-3</sup>, 1 × 10<sup>-4</sup>, and 1 × 10<sup>-5</sup> s<sup>-1</sup> until fracture on an Instron-type 4505 testing machine. The stress was determined from the cross-sectional area and the force measured with a 10 kN load cell. The strain was measured with a clip-on extensometer.

**Fatigue Tests:** The sample dimensions for fatigue testing are only slightly different from the tensile samples. The nominal cross section is 5 × 4 mm<sup>2</sup>, with the same principal outline. For better force application, the clamping surfaces are wider in relation to the measuring range, and the transition between them is less sharp. The specimens for the fatigue tests were mechanically ground to 4000 grit and afterward electrolytically

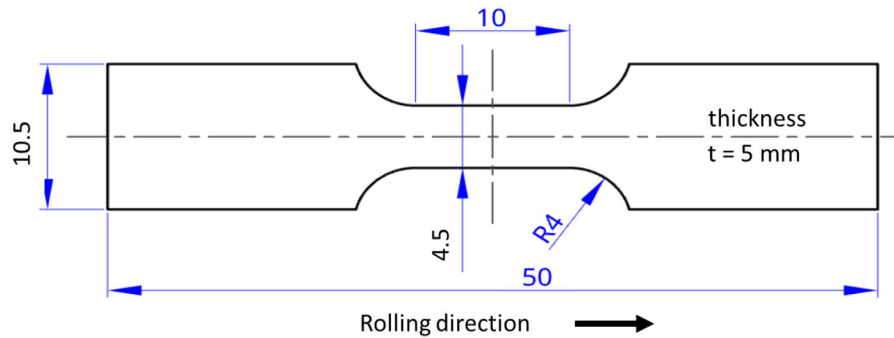


**Figure 12.** Geometry of tensile specimens.

polished. The fatigue tests were performed on an MTS 810, Material Testing Systems Corporation servo-hydraulic fatigue testing machine. Similar to the tensile testing, the stress was determined by a 10 kN load cell, and the strain was determined with a clip-on extensometer. To prevent the specimen from buckling, a constant tensile minimum strain of  $5 \times 10^{-5}$  was applied, and the total strain amplitude was varied between  $\Delta\epsilon_{\text{tot}}/2 = 1.2 \times 10^{-2}$  and  $\Delta\epsilon_{\text{tot}}/2 = 2.5 \times 10^{-4}$ . This resulted in a stress ratio  $R_\sigma$  of 0.42 to 0.20. The strain rate was  $2 \times 10^{-2} \text{ s}^{-1}$ . The number of cycles to failure was determined at a 20% decrease in stress amplitude from 1) half-life (in the case of cyclic softening) or 2) maximum stress amplitude (in the case of cyclic hardening).

## Acknowledgements

The authors gratefully acknowledge the financial support of the German Research Council (DFG) within the Cluster of Excellence Engineering of Advanced Materials, EXC 315. The authors are also very grateful to Mrs. N. Pfeffer for her valuable support in finalizing some of the diagrams.

## Conflict of Interest

The authors declare no conflict of interest.

## Keywords

interfaces mechanical properties, metallic laminates, ultrafine-grained and bimodal structures

Received: February 6, 2020

Revised: March 31, 2020

Published online:

- [1] H. Gleiter, in *Proc. of the 2nd Riso Int. Symp. on Metallurgy and Materials Science* (Eds: N. Hansen, A. Horsewell, T. Leffers, H. Lilholt), Risø Nat. Laboratory Roskilde, Denmark **1981**, pp. 15.
- [2] H. Gleiter, *Prog. Mater. Sci.* **1989**, *33*, 223.
- [3] Y. Saito, N. Tsuji, H. Utsunomiya, T. Sakai, R. G. Hong, *Scr. Mater.* **1998**, *39*, 1221.
- [4] Y. Saito, H. Utsunomiya, N. Tsuji, T. Sakai, *Acta Mater.* **1999**, *47*, 579.
- [5] N. Tsuji, N. Kamikawa, H. W. Kim, Y. Minamino, in *Ultrafine Grained Materials III* (Eds: Y. T. Zhu, T. G. Langdon, R. Z. Valiev, S. L. Semiatin, D. H. Shin, T. C. Lowe), TMS, Warrendale, PA, USA **2004**, p. 219.
- [6] M. Ruppert, W. Böhm, H. Nguyen, H. W. Höppel, M. Merklein, M. Göken, *J. Mater. Sci.* **2013**, *48*, 8377.

- [7] X. Huang, N. Tsuji, N. Hansen, Y. Minamino, *Mater. Sci. Eng. A* **2003**, *340*, 265.
- [8] W. Blum, X. H. Zeng, *Acta Mater.* **2009**, *57*, 1966.
- [9] R. Z. Valiev, I. V. Alexandrov, *J. Mater. Res.* **2002**, *17*, 5.
- [10] H. W. Höppel, J. May, P. Eisenlohr, M. Göken, *Z. Metallkd.* **2005**, *96*, 566.
- [11] J. May, H. W. Höppel, M. Göken, *Mater. Sci. Forum* **2006**, *503–504*, 781.
- [12] H. W. Höppel, J. May, M. Göken, *Adv. Eng. Mater.* **2004**, *6*, 781.
- [13] H. S. Kim, W. S. Ryu, M. Janacek, S. C. Baik, Y. Estrin, *Adv. Eng. Mater.* **2005**, *7*, 43.
- [14] N. Takata, S. H. Lee, C. Y. Lim, S. Kim, N. Tsuji, *J. Nanosci. Nanotechnol.* **2007**, *7*, 3985.
- [15] J. Bach, M. Stoiber, L. Schindler, H. W. Höppel, M. Göken, *Acta Mater.* **2020**, *186*, 363.
- [16] D. R. Lesuer, C. K. Syn, O. D. Sherby, J. Wadsworth, J. J. Lewandowski, W. H. Hunt, *Int. Mater. Rev.* **1996**, *41*, 169.
- [17] N. Tsuji, in *Nanostructured Metals and Alloys* (Ed: S. Whang), Woodhead Publishing Ltd, Oxford **2011**, p. 40.
- [18] T. Hausöl, V. Maier, C. W. Schmidt, M. Winkler, H. W. Höppel, M. Göken, *Adv. Eng. Mater.* **2010**, *12*, 740.
- [19] F. Kümmel, B. Diepold, K. F. Sauer, C. Schunk, A. Prakash, H. W. Höppel, M. Göken, *Adv. Eng. Mater.* **2018**, *21*, 1800286.
- [20] X. Ma, C. Huang, J. Moering, M. Ruppert, H. W. Höppel, M. Göken, J. Narayan, Y. Zhu, *Acta Mater.* **2016**, *116*, 43.
- [21] C. X. Huang, Y. F. Wang, X. L. Ma, S. Yin, H. W. Höppel, M. Göken, X. L. Wu, H. J. Gao, Y. T. Zhu, *Mater. Today* **2018**, *21*, 123.
- [22] P. Chekhonin, B. Beausir, J. Scharnweber, C.-G. Oertel, T. Hausöl, H. W. Höppel, H.-G. Brok-meier, W. Skrotzki, *Acta Mater.* **2012**, *60*, 4661.
- [23] A. Rollett, F. J. Humphreys, G. S. Rohrer, M. Hatherly, *Recrystallization and Related Annealing Phenomena*, 2nd ed., Pergamon, Oxford/New York **2004**.
- [24] M. Ruppert, C. Schunk, D. Hausmann, H. W. Höppel, M. Göken, *Acta Mater.* **2016**, *103*, 643.
- [25] L. Lienshöft, P. Chekhonin, D. Zöllner, J. Scharnweber, T. Marr, T. Krauter, H. W. Höppel, W. Skrotzki, *J. Mater. Res.* **2017**, *386*, 1.
- [26] H. Mughrabi, H. W. Höppel, M. Kautz, *Scr. Mater.* **2004**, *51*, 807.
- [27] Y. Estrin, A. Vinogradov, *Acta Mater.* **2013**, *61*, 782.
- [28] H. Mughrabi, H. W. Höppel, in *Structure and Mechanical Properties of Nanophase Materials-Theory and Computer Simulation vs. Experiment* (Eds: D. Farkas, H. Kung, M. Mayo, H. V. Swygenhoven, J. Weertman), Vol. 634, Materials Research Society, Warrendale PA **2001**, pp. B2.1.1–B2.1.12.
- [29] H. W. Höppel, H. Mughrabi, A. Vinogradov, in *Bulk Nanostructured Materials* (Eds: M. J. Zehetbauer, Y. T. Zhu), Wiley-VCH, Weinheim **2009**, p. 481.

- [30] A. Vinogradov, S. Hashimoto, in *Proc. of 2nd Int. Conf on Nanomaterials by severe plastic deformation Nanospd 2* (Eds: M. Zehetbauer, R. Z. Valiev), Wiley-VCH, Weinheim **2004**, p. 663.
- [31] H. W. Höppel, M. Göken, in *Nanostructured Metals and Alloys* (Ed: S. Whang), Woodhead Publishing, Cambridge, UK **2011**, p. 507.
- [32] H. Mughrabi, H. W. Höppel, *Int. J. Fatigue* **2010**, 32, 1413.
- [33] H. W. Höppel, M. Brunnbauer, H. Mughrabi, R. Z. Valiev, A. P. Zhilyaev, in *Materialsweek 2000 — Proc.* (Eds: Werkstoffwoche-Partnerschaft), Friedrich-Alexander-Universität Erlangen-Nürnberg (FAU), Frankfurt **2000**.
- [34] H. W. Höppel, R. Z. Valiev, *Z. Metallkd.* **2002**, 93, 641.
- [35] X. Jianga, Y. Bai, L. Zhang, G. Wu, S. Gao, X. Huang, N. Tsuji, *Mater. Sci. Eng. A* **2020**, 782, 139240.
- [36] C. Kwan, Z. Wang, S.-B. Kang, *Mater. Sci. Eng. A* **2008**, 480, 148.
- [37] A. H. Cottrell, B. Bilby, *Proc. Phys. Soc. London Sect. A* **1949**, 62, 49.
- [38] J. May, PhD Thesis, Friedrich-Alexander-Universität Erlangen-Nürnberg, **2005**.
- [39] H. Mughrabi, in *Dislocations and Properties of Real Materials*, The Institute of Metals, London **1985**, Vol. 323, pp. 244–262.
- [40] F. Kümmel, H. W. Höppel, M. Göken, *Mater. Sci. Eng. A* **2017**, 702, 406.
- [41] F. Kümmel, T. Hausöl, H. W. Höppel, M. Göken, *Acta Mater.* **2016**, 120, 150.
- [42] F. Kümmel, T. S. Tegtmeier, H. W. Höppel, M. Göken, I. O. P. Conf, *Mater. Sci. Eng.* **2017**, 194, 012036.